Applied Surface Science 493 (2019) 1195–1204

Contents lists available at ScienceDirect

Applied Surface Science

journal homepage: www.elsevier.com/locate/apsusc

Full length article

Investigation on the photocatalytic performance of $Ag_4P_2O_7$ microcrystals for the degradation of organic pollutants

Wyllamanney da S. Pereira[a], Cipriano B. Gozzo[a], Elson Longo[a], Edson R. Leite[a,b], Júlio C. Sczancoski[a,*]

[a] Universidade Federal de São Carlos (UFSCar), Department of Chemistry, São Carlos, SP, Brazil
[b] Brazilian Nanotechnology National Laboratory (LNNano), CNPEM, Campinas, SP, Brazil

ARTICLE INFO

Keywords:
Silver pyrophosphate
Photocatalysis
Photoluminescence
Organic dyes

ABSTRACT

The silver-based metal oxides have been considered good photocatalysts for the removal of organic dyes in wastewater treatments. In our knowledge, for the first time, the photoluminescence and photocatalytic properties of silver pyrophosphate ($Ag_4P_2O_7$) synthesized by the precipitation method have been investigated. The long- and short-range structural ordering was analyzed by means of X-ray diffraction and, Raman and infrared spectroscopies, respectively. The broadband photoluminescence spectrum revealed a typical profile arising from electronic transitions involving intermediary energy levels in the band gap. The photocatalytic efficiency of $Ag_4P_2O_7$ was monitored for the degradation of rhodamine B and 6G under ultraviolet light irradiation. The reusability and stability of this material as photocatalyst were checked by recycling tests. Different radical scavengers were introduced into reaction medium to detect the main active species involved in the degradation process of rhodamine 6G. Based on our results, a photodegradation mechanism for this synthetic organic dye by using $Ag_4P_2O_7$ photocatalyst was proposed in detail.

1. Introduction

The synthetic organic dyes are considered the most important compounds used to add or change the color of something [1]. These compounds have been widely employed in different industrial manufacturing segments, such as: cosmetic formulations [2], textile dyeing [3], food processing [4], leather tanning [5], paper printing [6], and color photography [7] and so on. A critical environmental problem is the inappropriate disposal of dye-containing wastewater generated in the industrial production lines into aquatic environments. As undesirable features, these kinds of dyes are potentially toxic, non-biodegradable or volatile, carcinogenic and mutagenic, bringing harmful risks to human health and irreparable damage to aquatic ecosystems [8–10]. The most traditional and important treatment methods employed to combat and minimize the toxic nature of these compounds are bacterial and fungal discoloration [11,12], membrane separation [13], electrochemical methods [14], coagulation [15] and photocatalysis [16–19]. For many researchers, the photocatalytic degradation is an emerging and efficient technology because it offers effective advantages for wastewater treatments, such as low cost, safe to handle, environmentally friendly reaction conditions, no sludge disposal, absence of secondary waste [20,21].

The photocatalysis refers to the acceleration of a light-induced reaction due to the presence of a semiconductor (photocatalyst) [22,23]. When the surface of a photocatalyst is exposed to light (energy similar or greater than the band gap energy of the photocatalyst), electrons are promoted from valence band (VB) to conduction band (CB), resulting in the appearance of electron/hole pairs. These charge carriers are available to induce redox activities with the chemical species adsorbed on the photocatalyst. The holes are able to oxidize donor molecules and react with water molecules to produce hydroxyl radicals. In contrast, the electrons react with oxygen to produce superoxide radicals. These free radicals trigger a series of chemical reactions that break down the dye macromolecules into smaller and less harmful substances (mineralization) [24–26]. A fundamental concept is that the photocatalytic efficiency of a semiconductor is dependent on the band gap, effective separation and recombination of photogenerated electron/hole pairs, surface-related adsorption properties, morphological aspects, porosity, chemical stability and reusability in aqueous medium [27–29].

Among the different types of semiconductors employed as photocatalysts, the silver-based metal oxides have demonstrated an excellent photocatalytic response for the degradation of synthetic organic dyes

* Corresponding author.
E-mail address: jcsfisica@gmail.com (J.C. Sczancoski).

https://doi.org/10.1016/j.apsusc.2019.07.148
Received 6 April 2019; Received in revised form 5 July 2019; Accepted 16 July 2019
Available online 17 July 2019

under ultraviolet/visible light irradiation [30–33]. However, few studies have been dedicated to silver pyrophosphate ($Ag_4P_2O_7$). Since the pioneering studies published by Takahashi et al. [34,35], the initial researches related to this material were mainly focused on the structural features, ionic conductivity, optical and dielectric properties [36–39]. With respect to photocatalytic activity, Zhao et al. [40] and Song et al. [41] verified a high functionality of pure $Ag_4P_2O_7$ phase and $Ag_4P_2O_7$-based composites for the degradation of methylene blue under visible light illumination.

In our knowledge, $Ag_4P_2O_7$ photocatalysts for the degradation of rhodamine B (RhB) and rhodamine 6G (Rh6G) have not been reported yet. Thus, in the present study, photocatalytic degradation of these organic dyes (as representative pollutants) under ultraviolet light irradiation was tested with $Ag_4P_2O_7$ synthesized by the precipitation method. The photocatalytic potential of this material was investigated in detail by means of the reusability and stability after three cycle runs. The main reactive species responsible for the photocatalytic degradation were identified with the addition of different radical scavengers in the system. Taking into account our experimental results, a photocatalytic mechanism for $Ag_4P_2O_7$ was proposed in detail. Moreover, the photoluminescence emissions at room temperature of this material were also explored.

2. Materials and methods

2.1. Synthesis

$Ag_4P_2O_7$ was synthesized by the precipitation method in aqueous medium by using potassium pyrophosphate ($K_4P_2O_7$, Aldrich, 99%) and silver nitrate ($AgNO_3$, Vetec, 99.8%) as chemical starting precursors. In a typical procedure, 50 mL of 8 mM $AgNO_3$ solution was mixed with 50 mL of 2 mM $K_4P_2O_7$ solution at room temperature under constant stirring for 10 min. The final solid precipitate was separated from the liquid phase via centrifugation (7000 rpm for 5 min), washed with deionized water and acetone (six times), and then dried in a lab oven at 60 °C for 2 h.

2.2. Characterization

The structural behavior of as-synthesized microcrystals was investigated by X-ray diffraction (XRD) by using a D8 Advance diffractometer (Bruker AXS, Germany) with CuKα radiation (λ = 0.154184 nm). Data were collected over 2θ ranging from 20° to 60° with a scanning scan rate and step size of 0.2°/min and 0.02°, respectively. The surface oxidation states and chemical composition of all samples were investigated by X-ray photoelectron spectroscopy (XPS) in an ESCA + spectrometer (ScientaOmicron, Germany) with a high-performance hemispheric analyzer (EA 125). The monochromatic Al*Kα* radiation (1486.6 eV) was used as an excitation source. The operating pressure in the ultrahigh vacuum chamber during the XPS analysis was maintained at around 2×10^{-9} mbar. The survey and high-resolution spectra were recorded with energy steps of 0.5 and 0.05 eV, respectively. The binding energies in all XPS spectra were calibrated in reference to C1s peak (284.8 eV). XPS spectra were examined with the CasaXPS software [42], in which the core-level signals were individually fitted with Gaussian-Lorentzian functions and background subtraction according to the Shirley method. Raman spectrum was collected by using a LabRAM HR800 spectrometer (Horiba Jobin Yvon, Japan) equipped with CCD detector (model DU420A-OE-325) and helium-neon (HeNe) laser (λ = 632.8 nm). The infrared absorption (IR) spectrum was acquired on an Equinox 55 Fourier-transform infrared spectrometer (Bruker Optics, Germany), in which the $Ag_4P_2O_7$ powder was mixture with potassium bromide. The morphological features were verified in an Inspect F50 scanning electron microscope equipped with Schottky Field Emission source (SEM) (Philips-FEI, Netherlands). The particle size distribution was estimated from SEM images by using the ImageJ software [43]. Ultraviolet-visible (UV–vis) spectrum was taken on a Cary 5G spectrophotometer (Varian, USA) operated in diffuse-reflection mode. The photoluminescence emission was measured at room temperature by using a Monospec 27 monochromator (Thermo Jarrell Ash, USA) coupled to a R955 photomultiplier (Hamamatsu, Japan). A krypton ion laser (model Innova 200, Coherent, USA) (λ = 350 nm) was used as an excitation source. The incident laser power on the sample was maintained at 15 mW.

2.3. Photocatalytic activity

The photocatalytic activity of $Ag_4P_2O_7$ under ultraviolet (UV) illumination was explored for the degradation of RhB and Rh6G. For these tests, 50 mg of $Ag_4P_2O_7$ were dispersed in 50 mL of 1×10^{-5} M dye solution via ultrasonic bath (model 1510, Branson, USA) on a frequency of 42 kHz for 15 min. Before UV illumination, the resulting suspension was placed inside the photoreactor and maintained under constant stirring in the dark for 30 min to reach the adsorption/desorption equilibrium. The first aliquot was collected as zero time reading. Then, the reaction medium was completely illuminated with four UV lamps (Philips TUV 15W SLV/25, maximum intensity at 254 nm) and maintained at 20 °C by means of a thermostatic circulating water bath. Aliquots of 1 mL were collected at regular intervals and posteriorly centrifuged (13,800 rpm for 20 min) to separate the precipitates from the dye solution. The photocatalytic reaction progress was monitored by recording variations in the maximum absorption band (554 nm for RhB; 526 nm for Rh6G) by using a V-660 UV–vis spectrophotometer (Jasco, Japan). After taking its UV–vis spectrum, each of the measured aliquots was transferred back to the reaction medium (avoiding to reduce the volume of the system). The stability and reusability of the photocatalyst was tested by three cycle runs for the degradation of Rh6G.

Different radical scavengers, including isopropanol (ISO) (99.5%, Synth), p-benzoquinone (BQ) (99%, Merck), and di-ammonium oxalate monohydrate (AOx) (99.5%–101%, Merck) were added into Rh6G solution containing the $Ag_4P_2O_7$ photocatalyst to capture hydroxyl radicals ($OH\cdot$), superoxide radicals ($O_2\cdot^-$), and holes (h^+), respectively. The molar concentrations of all scavengers adopted in the photocatalytic experiments were 0, 1 and 5 mM.

3. Results and discussion

3.1. Structural analysis

Fig. 1 shows a typical XRD pattern of as-synthesized $Ag_4P_2O_7$. A remarkable feature in this diffractogram was the presence of well-defined peaks, a typical attribute of solids with long-range structural ordering [44]. Therefore, the precipitation reaction at room temperature was a successful chemical route in the preparation of crystalline $Ag_4P_2O_7$ without any further heat treatment. Among all diffraction peaks, the most intense ones found at 2θ scattering angles of 27.1°, 28.8°, and 32.4° are belonging to hexagonal phase (available in Joint Committee on Powder Diffraction Standards (JCPDS) database n° 37-0187). No diffraction peaks related to metallic Ag or other secondary phases were detected. Our diffractogram is consistent with previous reports [38,41,45]. Additional information on crystallographic parameters (lattice constants and unit cell volume) and conformation of Ag and P clusters in this phosphate is currently a challenging task due to lack of structural data for this material. According to a study published in 1983 by Yamada and Koizumi [36], $Ag_4P_2O_7$ crystals grown by Czochralski method were well-described by a trigonal crystal system at room temperature, containing the lattice constants $a = 0.9538$ and $c = 4.083$ nm.

As a complementary technique, the Raman spectroscopy was employed as a characterization tool to monitor the local order as well as identify the vibrational modes of this material. Based on Raman spectra

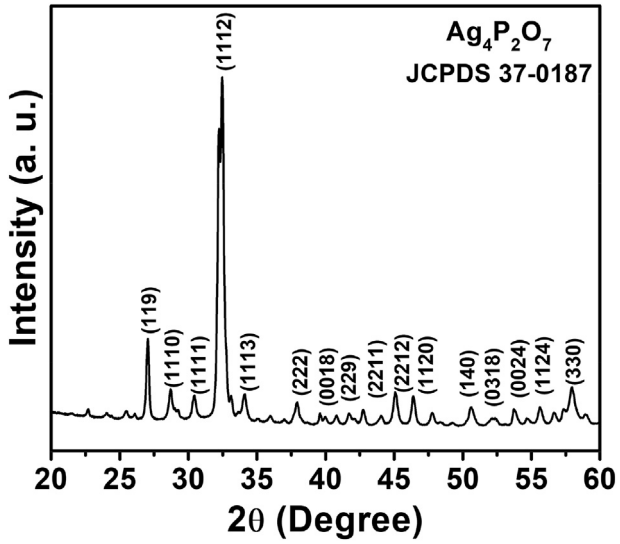

Fig. 1. XRD pattern of $Ag_4P_2O_7$.

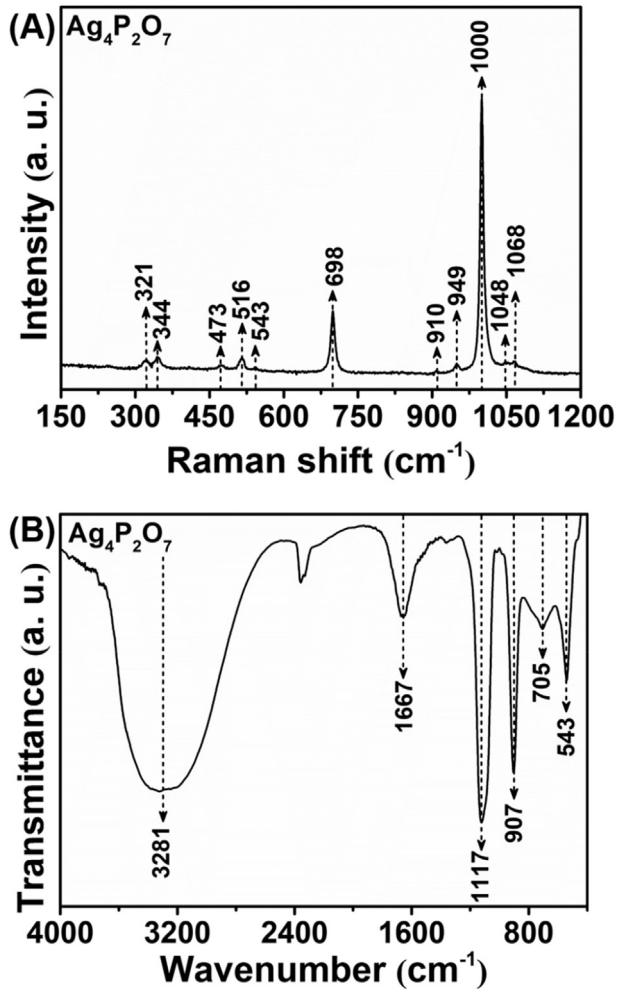

Fig. 2. (A) Raman and (B) IR spectra of $Ag_4P_2O_7$.

of other pyrophosphates found in previous papers [46–49], the corresponding positions of Raman-active bands detected in $Ag_4P_2O_7$ were identified. Generally, $P_2O_7^{4-}$ species have typical vibration frequencies associate to PO_3 groups and P-O-P bridge in the lattice. In our spectrum (Fig. 2A), the three bands located at 1000, 1048, and 1068 cm^{-1} are arising from $\nu_s PO_3$, while the others at 698, 910, and 949 cm^{-1} are due to $\nu_{as}PO_3$ and $\nu_s PO_3$, respectively. The $\delta_{as}PO_3$ vibrational modes were identified at 473, 516, and 543 cm^{-1}. The external modes assigned to rotational and translational movements of $P_2O_7^{4-}$ species were observed at 321 and 324 cm^{-1}. For a complete analysis, theoretical calculation can be an effective approach to validate these Raman-active modes. As this Raman spectrum exposed a profile with intense and well-defined bands, this material also is characterized by a short-range structural ordering [44].

In addition, IR spectroscopy was employed to extract any extra structural information of $Ag_4P_2O_7$. According to other published studies [45,48,50,51], the fundamental vibrational bands of pyrophosphates are arising from $P_2O_7^{4-}$ species, normally observed over a frequency range from 500 to 1280 cm^{-1}. In our case, four IR-active bands were found at 543, 705, 907 and 1117 cm^{-1}, which were ascribed to $\delta_{as}PO_3$, $\nu_s POP$, $\nu_{as}POP$, and $\nu_s PO_3$, respectively (Fig. 2B). The two broad bands at 1667 and 3281 cm^{-1} are related to H—O bending and H—O asymmetry stretching modes of water molecules adsorbed on the surface of as-prepared samples, respectively [52].

The nature of the chemical surface is one of the crucial points that influences the photocatalytic properties; therefore, XPS technique is a good alternative to identify the chemical composition and element valence states on the surfaces of $Ag_4P_2O_7$. Fig. 3A shows a representative XPS survey spectrum, which clearly demonstrated the existence of Ag, C, O and P in the samples. The C 1s peak is attributed to the widespread presence of carbon in the environment. In relation to Ag 3d core level, the appearance of a well-resolved doublet Ag $3d_{3/2}$ and Ag $3d_{5/2}$ bands was detected at around 374 and 368 eV, respectively. Two Gaussian-Lorentzian functions (G-L peaks) were sufficiently able to fit each of these bands, suggesting a coexistence of Ag^0 and Ag^+ species (Fig. 3B). Thus, the peaks at 373.8 eV and 367.7 eV are attributed to Ag^+ of Ag clusters in $Ag_4P_2O_7$ and those at 374.3 eV and 368.4 eV are ascribed to Ag^0 [37,53]. The corrected areas of each peak are proportional to the number of atoms of a specific element present on the surface of a material. Therefore, the areas corresponding to Ag 3d core level are able to predict the Ag^0 and Ag^+ contents on the surface of $Ag_4P_2O_7$. The area data revealed an Ag^0 concentration of approximately 41.1 at.%. On the other hand, XRD pattern did not show any evidence of Ag^0 in $Ag_4P_2O_7$ (Fig. 1). According to these results, Ag^0 signals detected in our spectrum can be arising from X-ray light irradiation during the XPS measurements.

The O 1s core level was perfectly fitted into two G-L peaks detected at 530.06 eV and 532.1 eV, corresponding to P—O bonds in the hexagonal lattice and hydroxyl groups (H—O) chemisorbed on the surface, respectively (Fig. 3C) [54,55]. For P 2p core level, the band detected at binding energy of 133.2 eV was ascribed to P^{5+} oxidation state (Fig. 3D) [56,57].

3.2. Morphological aspects

SEM was employed to explore the morphological features of $Ag_4P_2O_7$. Low-magnification SEM image identified a large amount of hexagonal plate-like microparticles with smooth surfaces (Fig. 4a). This particle shape has also been verified in diverse metal oxides synthesized with/without the introduction of chemical additives or surfactants to the reaction medium [58–60]. Based on this observation, we presume that the growth proceeded according to a homogeneous nucleation process (classical crystallization theory). In this phenomenon, the nucleation occurs spontaneously and randomly when a supersaturation regime is reached. Once supersaturated, the primary particles can grow from solution [61]. After growth stage, these particles are able to aggregate via van der Waals attractive forces [62]. Due to the appearance of smooth surfaces in $Ag_4P_2O_7$ microcrystals, the last stage of the growth kinetics occurred through Ostwald ripening mechanism, which involves the transfer of atoms from smaller and less stable particles to larger ones [63].

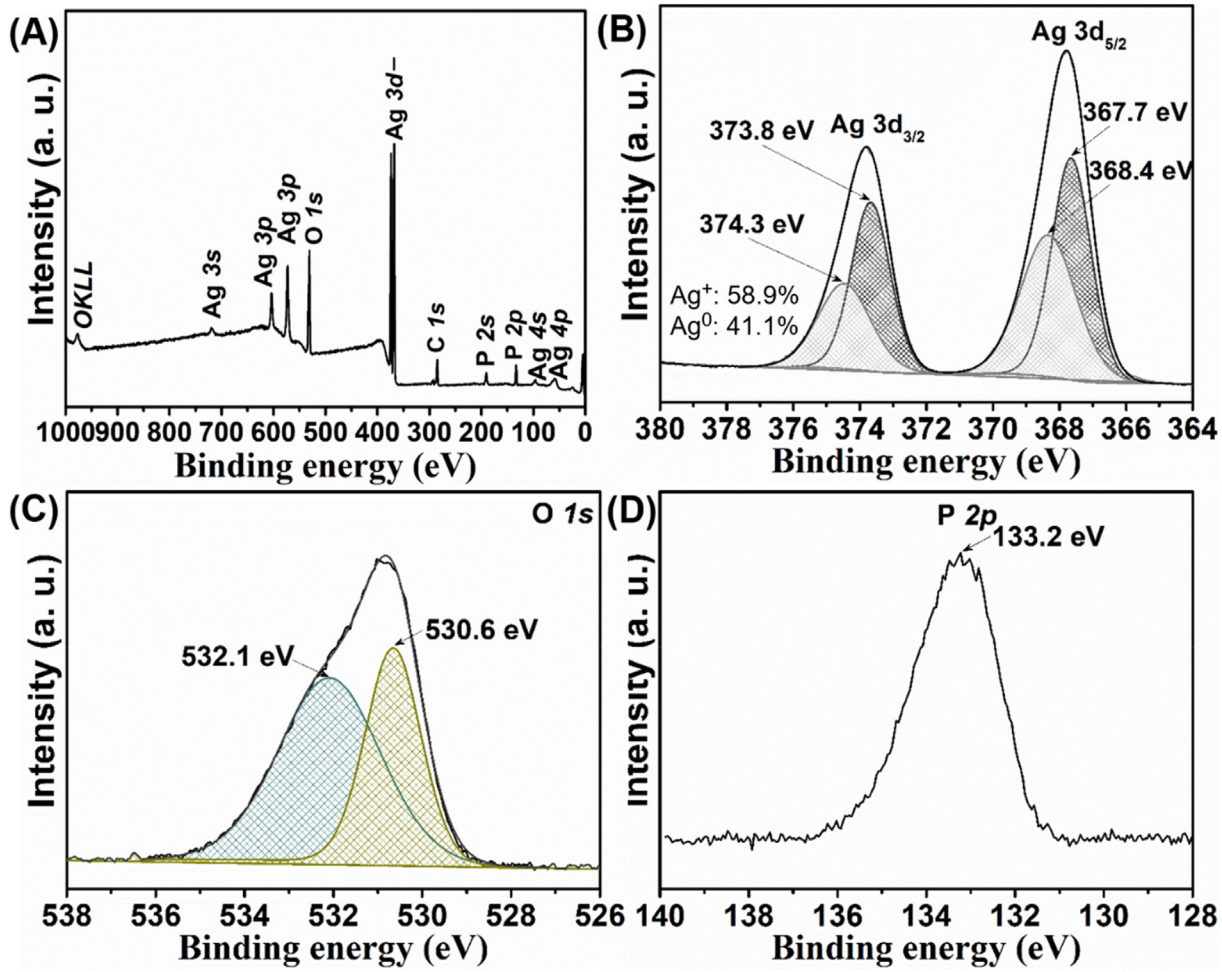

Fig. 3. (A) XPS survey spectrum of $Ag_4P_2O_7$ and high-resolution (B) Ag 3d, (C) O 1 s, and (D) P 2p core level spectra, respectively.

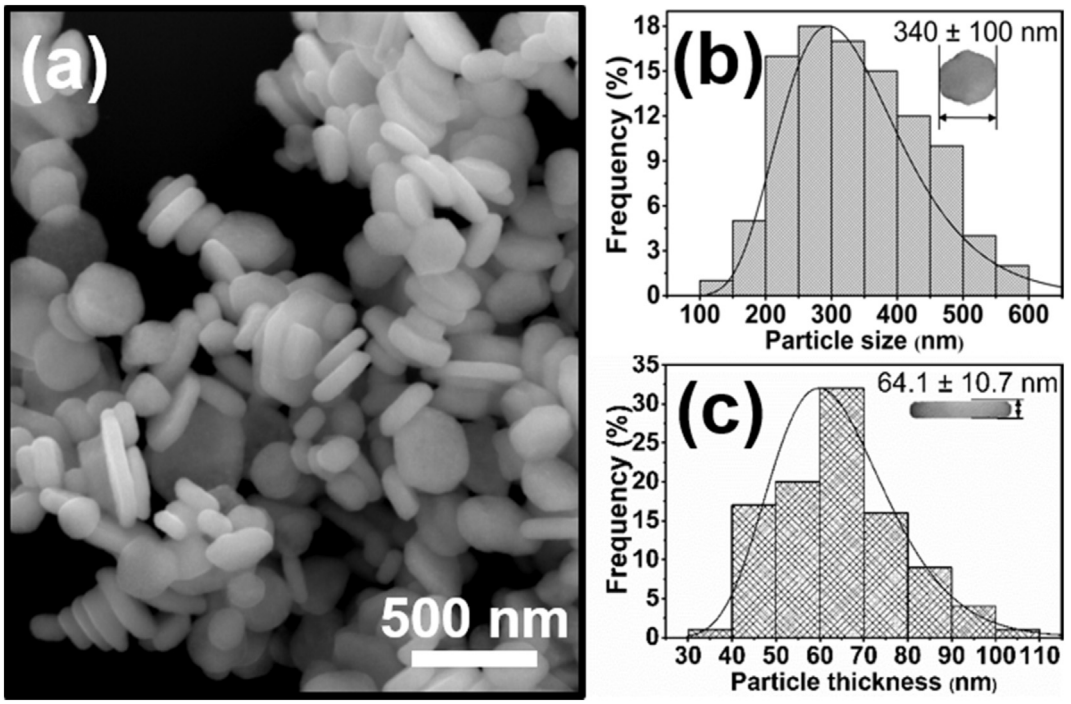

Fig. 4. (a) Low-magnification SEM image and, (b–c) average particle size and thickness distributions of $Ag_4P_2O_7$, respectively.

Performing a statistical analysis, a particle size distribution histogram was obtained by measuring the dimensions (size and thickness) of 100 particles from SEM images. As deduced by fitting the size distribution with a log-normal function, the average crystal size and thickness were estimated at 0.34 μm and 64.1 nm, respectively (Fig. 4b–c).

3.3. Optical band gap and photoluminescence emissions

Band gap, energy difference between the top of the valence band (VB) and the bottom of the conduction band (CB), is a critical parameter responsible for the performance of the electronic, optical, redox, and transport (electrical) properties in the materials [64]. From the point of view of photoluminescence and photocatalytic properties in ceramic semiconductors, the optical band gap energy (E_g) plays a key role in determining the minimum excitation wavelength to promote the appearance of electron/hole pairs. These charge carriers effectively contribute to photoluminescence emissions as well as in redox activities for the degradation of organic pollutants. Another important factor with respect to the band structure of semiconductors is that the kind and concentration of intrinsic defects (bulk, surface and interface) cause a local perturbation in the structure, introducing new acceptor and/or donor levels in the forbidden region. These energy levels are well-known as deep- and shallow-level defect states [65,66].

An efficient and alternative strategy adopted to estimate E_g of crystalline semiconductors is by means of the UV–vis spectroscopy. A typical UV–vis diffuse reflectance spectrum of $Ag_4P_2O_7$ is illustrated in Fig. 5A. Hirono et al. [37] reported that the E_g of this material is characterized by an indirect optical band gap. By employing the Kubelka-Munk method [67] for indirect allowed electronic transitions, an E_g value of approximately 3.38 eV was found for this pyrophosphate. This value is in good agreement with other published papers [37,41].

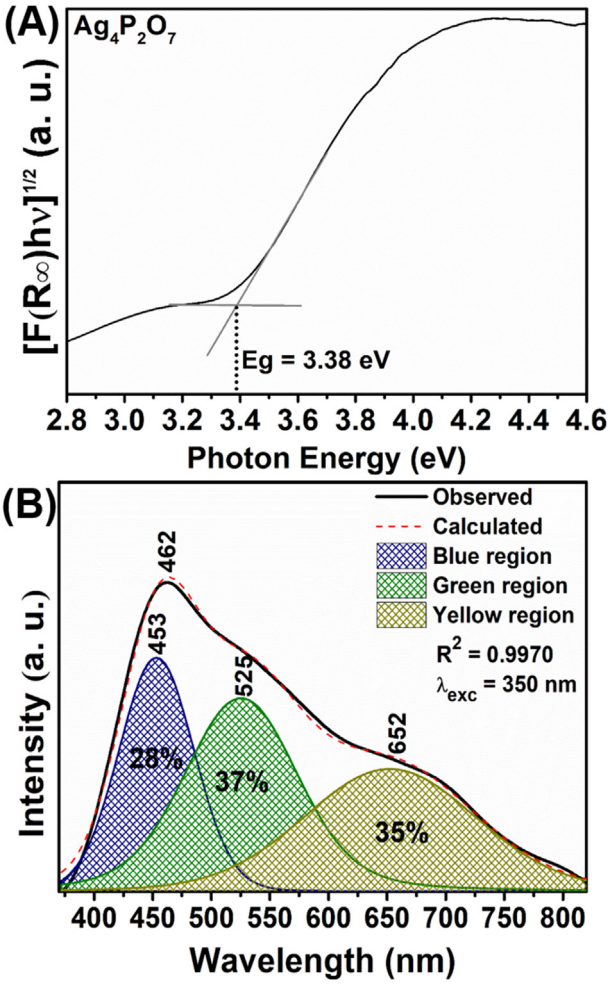

Fig. 5. (A) UV–vis reflectance spectrum and (B) deconvoluted photoluminescence spectrum of $Ag_4P_2O_7$.

The Mulliken electronegativity theory [68] was employed in our study to clarify the CB and VB edge positions in $Ag_4P_2O_7$ by means of the Eqs. (1) and (2).

$$E_{VB} = \chi - E_e + 0.5E_g \quad (1)$$

$$E_{CB} = E_{VB} - E_g \quad (2)$$

where χ is the electronegativity of the semiconductor, E_g is the band gap of the semiconductor, E_e is the energy of free electrons vs hydrogen (4.5 eV) [69], E_{CB} and E_{VB} are the conduction and valence band edge potentials, respectively. In these equations, by using $\chi = 6.12$ [70], $E_e = 4.5$ eV, $E_g = 3.38$ eV, E_{VB} and E_{CB} of $Ag_4P_2O_7$ were calculated at −0.07 and 3.31 eV, respectively.

In terms of photoemission properties, the broadband photoluminescence spectrum of $Ag_4P_2O_7$ is a typical behavior of the involvement of several energy levels during the electronic transitions (Fig. 5B). To qualitatively identify the contribution of these energy levels, this spectrum was deconvoluted and perfectly fitted by using the Pseudo-Voigt function. As a result, three distinct regions correlated to visible light emission centers were registered, including: blue (453 nm = 2.73 eV), green (525 nm = 2.36 eV), and yellow (652 nm = 1.90 eV). Pondering each region individually (area %), the values found in ascending order were: blue (28%) < yellow (35%) < green (37%). Conceptually, the origin of yellow, orange, and red emissions are ascribe to deep-level defect states, while the shallow-level defect states are responsible for violet and blue emissions [71]. Taking into account this confirmation, our photoluminescence data exposed a greater participation of deep-level defect states in relation to shallow-level defect states. Moreover, due to the excitation wavelength chosen in this experiment (350 nm = 3.54 eV), band-to-band recombination processes also significantly contributed to the recombination of electron/hole pairs.

3.4. Photocatalytic property

The photocatalytic efficiency of $Ag_4P_2O_7$ was tested for the degradation of two organic dyes (RhB and Rh6G) under UV light illumination. All photocatalytic processes were carefully monitored by measuring the maximum absorption bands of these dyes (λ_{RhB} = 554 nm and λ_{Rh6G} = 526 nm) at predetermined time intervals via UV–vis spectroscopy, as illustrated in Fig. 6.

Insets in Fig. 6A–B show the molecular structures of RhB and Rh6G, respectively. The intense absorption band centered at 554 nm for RhB, commonly detected in UV–vis spectroscopy, is originate from π-π* transitions (i.e., N,N,N′,N′-tri-tetraethylated rhodamine molecule) from binding HOMO to anti-binding LUMO along the longest dimension of the conjugated system. The presence of a shoulder at 521 nm is often related to the dimmer of RhB [72]. On the other hand, the absorption maximum band at 526 nm as well as the shoulder at 496 nm for Rh6G correspond to H-aggregates of the dye associated to π-π* transitions [73,74]. This type of aggregation consists in transition moment largely parallel to the long axis of the molecule, forming a nearly vertical stack [75].

Analyzing the UV spectra of RhB and Rh6G without the photocatalyst (Fig. 6A–B), a photolysis of 14% for RhB and 4% for Rh6G was observed after 70 min and 25 min exposure to UV light illumination, respectively. In the presence of $Ag_4P_2O_7$ photocatalyst, a reduction of the maximum absorption band in both RhB and Rh6G was noted when the exposure time to ultraviolet irradiation was increased (Fig. 6C–D). The highest photocatalytic activity of $Ag_4P_2O_7$ was achieved for Rh6G solution, which was able to degrade 99% of this dye after 25 min

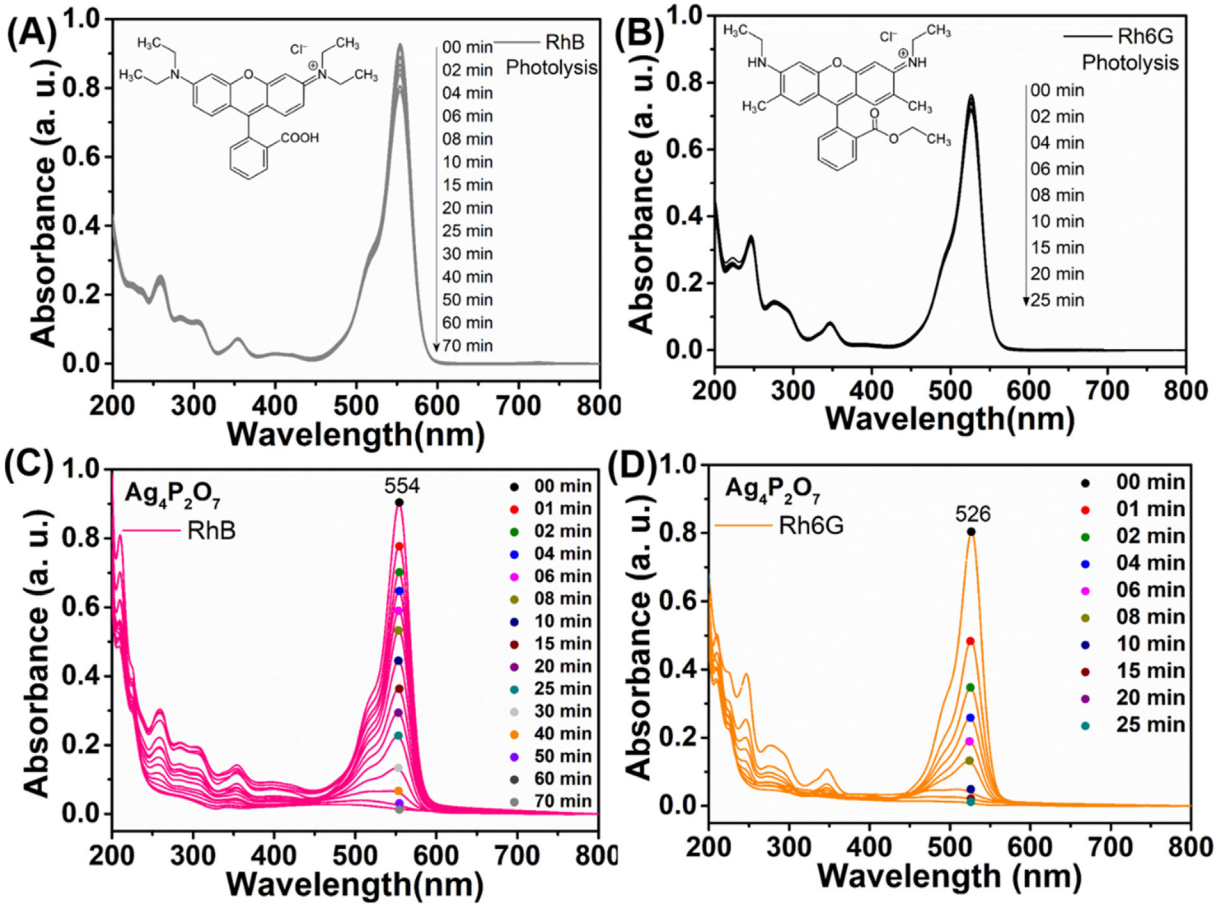

Fig. 6. Evolution of UV–vis spectra for the degradation of RhB and Rh6G under UV illumination without (A–B) and with $Ag_4P_2O_7$ photocatalyst (C–D), respectively.

(Fig. 6D). On the other hand, 70 min were required for this photocatalyst to degrade 98% of RhB solution (Fig. 6C). In particular, the degradation process of RhB is based on an oxidative attack by active oxygen species on both N-ethyl group and aromatic chromophore ring, causing a decrease of the maximum absorption band ($\lambda = 554$ nm), i.e., photodiscoloration of the dye [76,77]. Another relevant concept is that the shifting in the maximum absorption band implies the formation of intermediates during the photodegradation reaction, such as N,N,N′-triethylated rhodamine ($\lambda = 539$ nm), *N,N′*-di-ethylated rhodamine ($\lambda = 522$ nm), N-ethylated rhodamine ($\lambda = 510$ nm) and rhodamine ($\lambda = 498$ nm) [78–80]. In our study, the photodecoloration process of pollutant molecules was attributed to the intrinsic photooxidative activity of $Ag_4P_2O_7$ photocatalyst, without the presence of any intermediate specie detected in the visible absorption spectrum. Conceptually, key variables as adsorption capacity, size and type of active sites have direct influence in the selective degradation of organic pollutants [78,81,82]. Hence, molecular selective activity of $Ag_4P_2O_7$ microcrystals yielded a better photocatalytic performance for the degradation of Rh6G than RhB.

The reaction kinetics responsible for the degradation of RhB and Rh6G, with and without photocatalysts, were well-described by a pseudo-first order rate law (Fig. 7A–B), as expressed by the following equation [83]:

$$-\ln(C_t/C_0) = kt \quad (3)$$

where k is the reaction rate constant, t is the time, C_t and C_0 are the concentrations at time t and 0 of the organic dye, respectively. The k values (min^{-1}) were graphically determined from the slope of $-\ln(C_t/C_0)$ as a function of the irradiation time (Fig. 7C–D). In this case, for the degradation processes of RhB and Rh6G were estimated k values of $0.0573\ min^{-1}$ ($R^2 = 0.9841$) and $0.1845\ min^{-1}$ ($R^2 = 0.9950$), respectively.

In a traditional photocatalytic experiment, reactive species are the main agents responsible for the degradation of organic pollutants. Usually, photoinduced species, including holes (h^+), hydroxyl radicals ($OH\cdot$), and superoxide radicals ($O_2\cdot^-$), are expected to be involved in heterogeneous photocatalytic reactions under appropriate light irradiation [84]. To facilitate the identification of which species were effective in the photodegradation process, different radical scavengers (ISO, BQ, and AOx) were added into Rh6G solution [85]. The final photodegradation data with the use of scavengers are shown in Fig. 7E. Independent of the scavenger concentration, the AOx and BQ strongly interfered in the photocatalytic process mediated by $Ag_4P_2O_7$, except the ISO. Therefore, h^+ and $O_2\cdot^-$ active species presented a greater participation as oxidative agents during the photocatalysis. When compared to the standard TiO_2 powder commercially available (Degussa P25), the photocatalytic performance of $Ag_4P_2O_7$ exhibited a similar effectiveness for the degradation of Rh6G under UV light irradiation (Fig. 7F).

From the technological perspective for the wastewater treatment, the chemical stability is an essential parameter to quantify how many times a photocatalyst can be reused without significant losses of its photocatalytic properties. Hence, recycling photocatalytic experiments were performed for $Ag_4P_2O_7$ photocatalyst (Fig. 8). In a first observation, there is a notable reduction in the photocatalytic performance from one cycle run to another. In relation to first cycle run, it was noted reductions of 43% and 52% in the photocatalytic effectiveness for the second and third cycle runs, respectively (Fig. 8A). To ensure a better understanding on this behavior, XRD, XPS and SEM techniques were employed to identify some structural and morphological change in

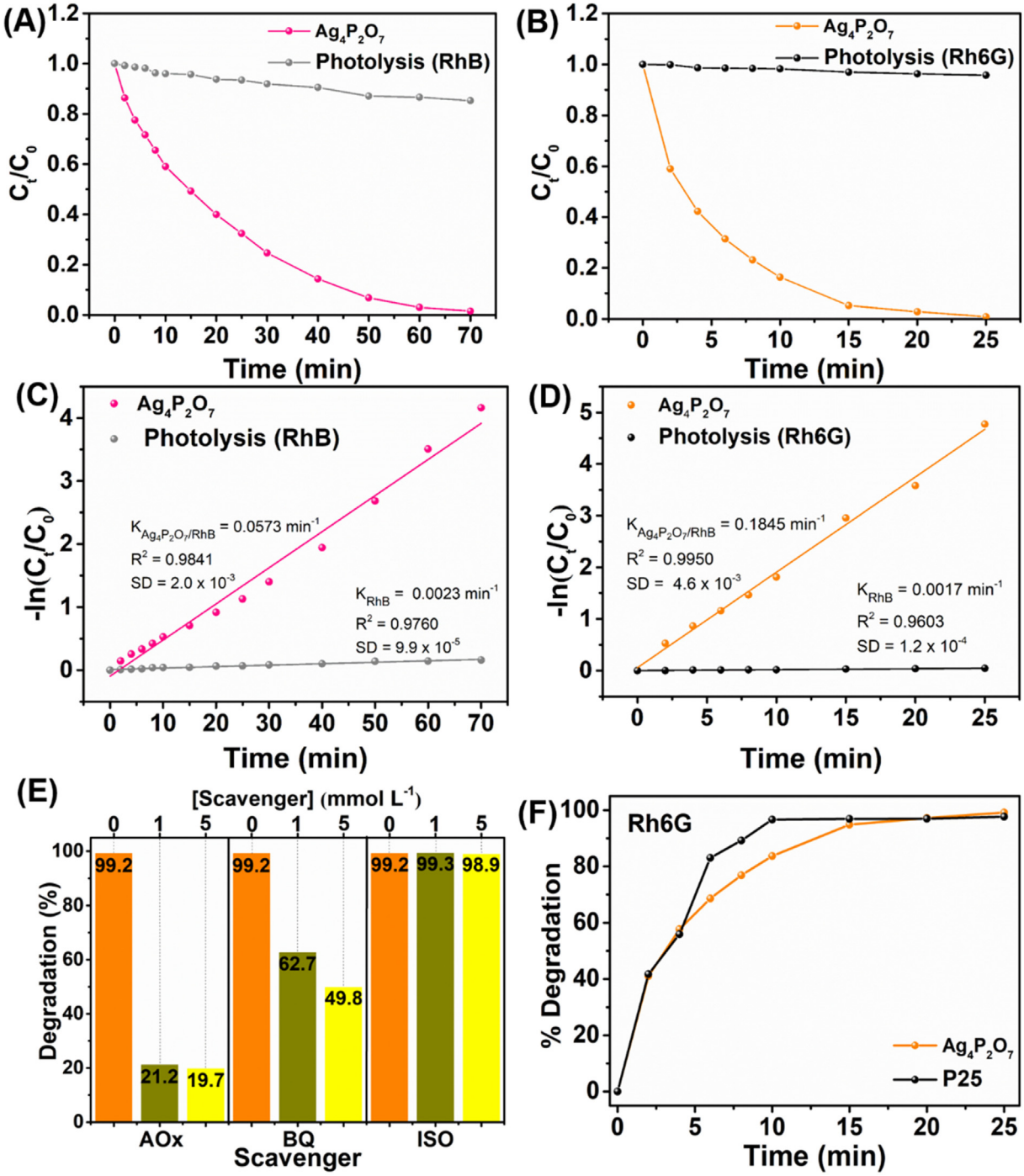

Fig. 7. (A–B) Photocatalytic activity and (C–D) pseudo-first order kinetics for the degradation of RhB and Rh6G under UV illumination without and with $Ag_4P_2O_7$ photocatalyst, respectively; (E) photodegradation rates of Rh6G by using the $Ag_4P_2O_7$ photocatalyst in the presence of distinct active radical scavengers (AOx, BQ, and ISO) at different concentrations (0, 1 and 5 mmol L^{-1}); (F) comparative analysis between P25 (commercial standard) and $Ag_4P_2O_7$ photocatalyst for the degradation of Rh6G.

$Ag_4P_2O_7$ after the photocatalysis tests.

Even after three run cycles, XRD patterns of $Ag_4P_2O_7$ presented typical reflection peaks ascribed to hexagonal phase without the identification of other additional phases (especially, metallic Ag) (Fig. 8B). This structural stability can be corroborated with the high-resolution XPS spectrum for Ag 3d core level acquired for the sample submitted to the third run cycle. In this case, the corrected peak areas corresponding to Ag^0 concentration on the surface of $Ag_4P_2O_7$ are very similar before and after the recycling tests (~41 at.%) (Figs. 3B and 8C). On the other hand, low-magnification SEM images demonstrated that the $Ag_4P_2O_7$ microcrystals lost their hexagonal plate shape, i.e., the recycling processes provoked a morphological damage (Figs. 4a and 8C). Consequently, the defects generated by this phenomenon acted as trapping centers of electron/hole pairs, affecting the availability of charge carriers responsible for the degradation of Rh6G and suppressing the photocatalytic activity of $Ag_4P_2O_7$.

Considering all experimental analyses previously described, a photocatalytic mechanism was proposed for the photodegradation of Rh6G under UV illumination by employing $Ag_4P_2O_7$ as photocatalyst (Fig. 9). The electronic band structure of $Ag_4P_2O_7$ was based on the data

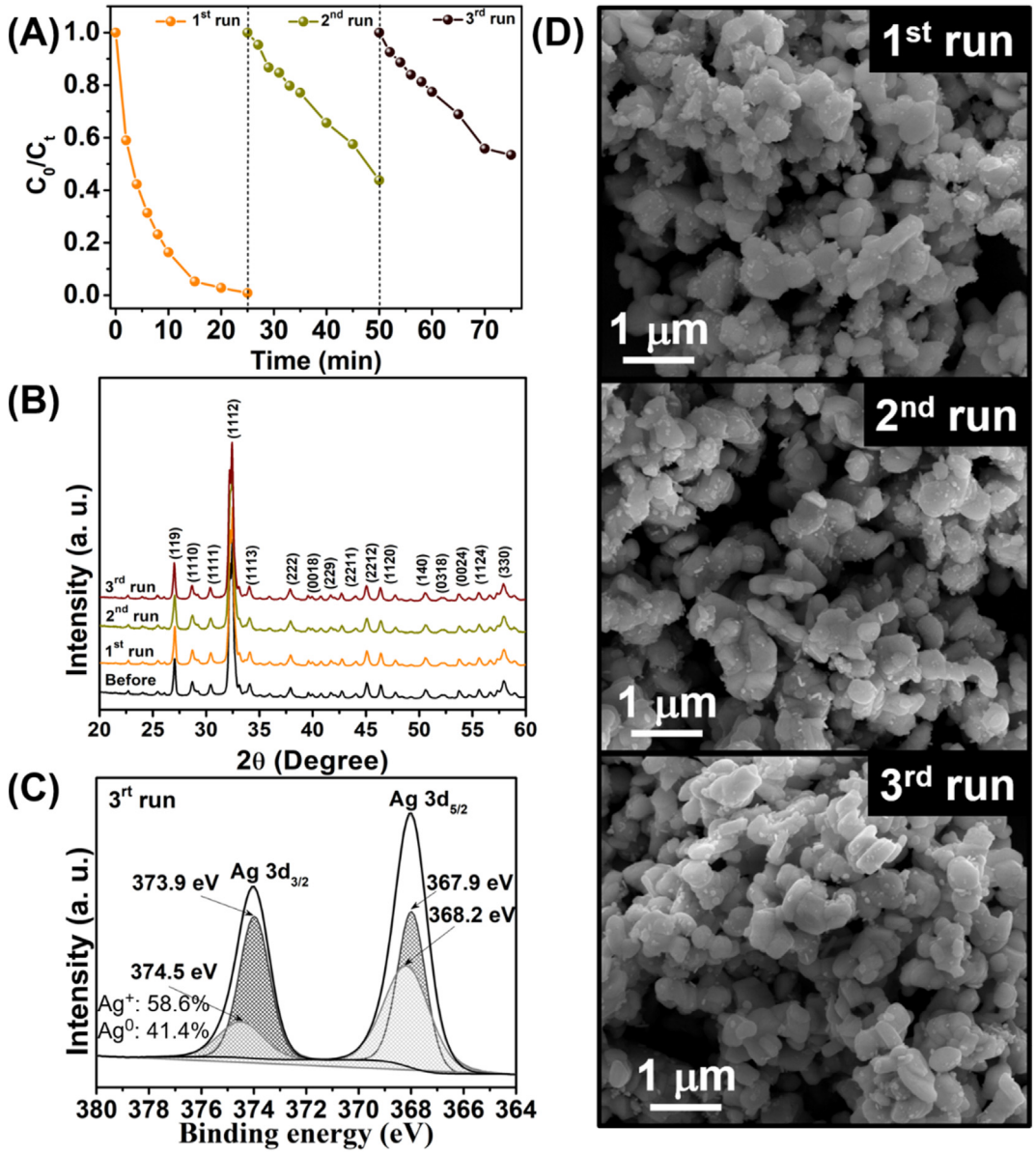

Fig. 8. (A) Cycle run curves by using $Ag_4P_2O_7$ photocatalyst for the degradation of Rh6G under UV illumination; (B) XRD patterns, (C) high-resolution Ag 3d core level spectrum (for the photocatalyst used in the third cycle run) and (D) SEM images of $Ag_4P_2O_7$ after recycling tests.

obtained for E_g (Kubelka-Munk method) [67] as well as for E_{CB} and E_{VB} values estimated by Eqs. (1) and (2) [68].

When irradiated with UV light, the optical excitation leads to the promotion of electrons (e^-) from VB to CB, leaving behind holes (h^+) in the VB (Eq. (4)). The excited electrons (e^-) can migrate towards the surface of the photocatalyst and react with the adsorbed oxygen, forming $O_2\cdot^-$ radicals (Eq. (5)). On the other hand, photogenerated holes (h^+) react with adsorbed H_2O to form hydroxyl radicals ($OH\cdot$) and proton (H^+) (Eq. (6)). These h^+ in the VB are able to effectively participate in the photodegradation process of the organic dye molecules via direct oxidation (formation of products (1)) and/or act together with $HO_2\cdot$ and $O_2\cdot^-$ to oxidize the dye in products (2) (Fig. 9). Another significant point is that hydroperoxyl radical ($HO_2\cdot$) (active specie in the photodegradation) can also be produced by the reaction between $O_2\cdot^-$ and H^+. All possible stages involved in the photodegradation of Rh6G are reported in the following equations:

$$Ag_4P_2O_7 + h\nu \rightarrow Ag_4P_2O_7\,(e^-_{CB} + h^+_{VB}) \quad (4)$$

$$Ag_4P_2O_7(e^-_{CB}) + O_{2(ads)} \rightarrow Ag_4P_2O_7 + O_2\bullet^- \quad (5)$$

$$Ag_4P_2O_7(h^+_{VB}) + H_2O_{(ads)} \rightarrow Ag_4P_2O_7 + H^+ + OH^\bullet \quad (6)$$

$$Ag_4P_2O_7(h^+_{VB}) + Rh6G \rightarrow Products\ 1 \quad (7)$$

$$Rh6G + Ag_4P_2O_7(h^+_{VB})/HO_2^\bullet/OH^\bullet \rightarrow Products\ 2 \quad (8)$$

4. Conclusion

In summary, $Ag_4P_2O_7$ was successfully synthesized by the precipitation method at room temperature. This synthetic route yielded the formation of several hexagonal plate-like microparticles. XRD pattern revealed that this material has a hexagonal phase, whose the presence of intense and defined diffraction peaks implied in a high degree of crystallinity. Raman and IR spectra exhibited typical vibration frequencies associated to PO_3 groups and P-O-P bridge arising from $P_2O_7^{4-}$ species. UV–vis spectrum presented a profile governed by indirect electronic transitions, in which E_g was estimated at around 3.38 eV. The maximum photoluminescence emission was detected in the blue region of the visible electromagnetic spectrum, confirming a

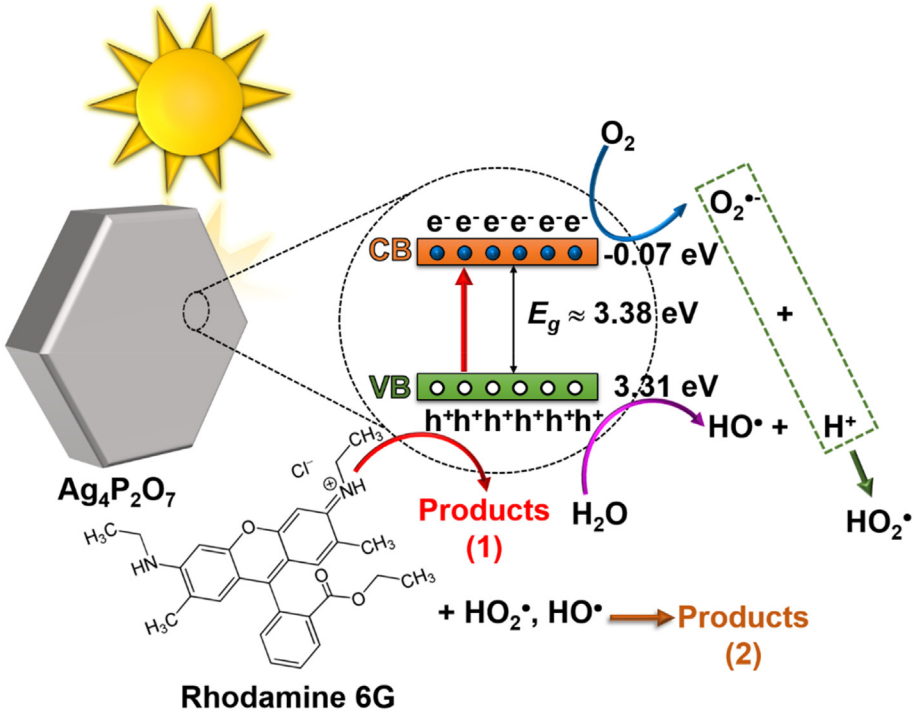

Fig. 9. Schematic photocatalytic mechanism by using $Ag_4P_2O_7$ photocatalyst for the photodegradation of Rh6G under UV illumination.

higher participation of shallow-level defect states in the forbidden region. In terms of photocatalytic property, $Ag_4P_2O_7$ presented a superior performance for the degradation of Rh6G (25 min) in relation to RhB (70 min). The use of radical scavengers into Rh6G solution revealed that the h^+ and $O_2\cdot^-$ active species have an effective participation in the photodegradation. Despite the structural stability, recycling tests showed a significant reduction in the photocatalytic efficiency of $Ag_4P_2O_7$. This behavior was ascribed to the appearance of several defects (traps of electron/hole pairs) in the microcrystals during cycle run stages. In particular, $Ag_4P_2O_7$ is promising candidate for the formation of heterostructures with other materials for purposes focused on the degradation of other contaminants under ultraviolet/visible irradiation.

Acknowledgments

The authors are grateful to FAPESP (2015/11917-8; 2016/23663-3; 2013/07296-2; 2012/14004-5), CNPq (153299/2015-0) and CAPES for the financial support. Special thanks to Prof. Dr. Maximo S. Li, Dr. João Batista Souza Junior and Prof. Dr. Valmor R. Mastelaro for their technical contributions in photoluminescence and XPS measurements, respectively.

References

[1] A. Gürses, M. Açıkyıldız, K. Güneş, M.S. Gürses, Dyes and Pigments, Springer International Publishing, 2016.
[2] Y. Xian, Y. Wu, X. Guo, Y. Lu, H. Luo, D. Luo, Y. Chen, Simultaneous determination of 11 restricted dyes in cosmetics by ultra high-performance liquid chromatography/tandem mass spectrometry, Anal. Methods 5 (2013) 1965.
[3] M. Iqbal, Textile Dyes, Rehbar, Karachi, 2008.
[4] B. Rohrig, Eating With Your Eyes: The Chemistry of Food Colorings, ChemMatters, 2015 October.
[5] O. Tünay, I. Kabdaşli, D. Orhon, G. Cansever, Use and minimization of water in leather tanning processes, Water Sci. Technol. 40 (1999) 237–244.
[6] W. Wang, N. Xie, L. He, Y. Yin, Photocatalytic colour switching of redox dyes for ink-free light-printable rewritable paper, Nat. Commun. 5 (2014) 5459.
[7] C.C. Van de Sande, Dye diffusion systems in color photography, Angew. Chem. Int. Ed. 22 (1983) 191–209.
[8] M. Solís, A. Solís, H.I. Pérez, N. Manjarrez, M. Flores, Microbial decolouration of azo dyes: a review, Process Biochem. 47 (2012) 1723–1748.
[9] International Agency for Research on Cancer, Some Aromatic Amines, Organic Dyes, and Related Exposures, IARC Press, International Agency for Research on Cancer, 2010.
[10] V. Khandegar, A.K. Saroha, Electrocoagulation for the treatment of textile industry effluent - a review, J. Environ. Manag. 128 (2013) 949–963.
[11] S.K. Sen, S. Raut, P. Bandyopadhyay, S. Raut, Fungal decolouration and degradation of azo dyes: a review, Fungal Biol. Rev. 30 (2016) 112–133.
[12] C. Pearce, The removal of colour from textile wastewater using whole bacterial cells: a review, Dyes Pigments 58 (2003) 179–196.
[13] C. Thamaraiselvan, N. Michael, Y. Oren, Selective separation of dyes and brine recovery from textile wastewater by nanofiltration membranes, Chem. Eng. Technol. 41 (2018) 185–293.
[14] E. Brillas, C.A. Martínez-Huitle, Decontamination of wastewaters containing synthetic organic dyes by electrochemical methods. An updated review, Appl. Catal., B 166-167 (2015) 603–643.
[15] A. Matilainen, M. Vepsalainen, M. Sillanpaa, Natural organic matter removal by coagulation during drinking water treatment: a review, Adv. Colloid Interf. Sci. 159 (2010) 189–197.
[16] Z. Wang, J. Lv, J. Zhang, K. Dai, C. Liang, Facile synthesis of Z-scheme $BiVO_4$/porous graphite carbon nitride heterojunction for enhanced visible-light-driven photocatalyst, Appl. Surf. Sci. 430 (2018) 595–602.
[17] Y. Huo, Y. Yang, K. Dai, J. Zhang, Construction of 2D/2D porous graphitic C_3N_4/SnS_2 composite as a direct Z-scheme system for efficient visible photocatalytic activity, Appl. Surf. Sci. 481 (2019) 1260–1269.
[18] J. Zhang, J. Lv, K. Dai, C. Liang, Q. Liu, One-step growth of nanosheet-assembled BiOCl/BiOBr microspheres for highly efficient visible photocatalytic performance, Appl. Surf. Sci. 430 (2018) 639–646.
[19] T. Hu, Y. Yang, K. Dai, J. Zhang, C. Liang, A novel Z-scheme Bi_2MoO_6/BiOBr photocatalyst for enhanced photocatalytic activity under visible light irradiation, Appl. Surf. Sci. 456 (2018) 473–481.
[20] P. Mahata, T. Aarthi, G. Madras, S. Natarajan, Photocatalytic degradation of dyes and organics with nanosized $GdCoO_3$, J. Phys. Chem. C 111 (2007) 1665–1674.
[21] K. Kabra, R. Chaudhary, R.L. Sawhney, Treatment of hazardous organic and inorganic compounds through aqueous-phase photocatalysis: a review, Ind. Eng. Chem. Res. 43 (2004) 7683–7696.
[22] R. Saravanan, F. Gracia, A. Stephen, Basic principles, mechanism, and challenges of photocatalysis, Nanocomposites for Visible Light-induced Photocatalysis, Springer, 2017, pp. 19–40.
[23] S. Kumar, W. Ahlawat, G. Bhanjana, S. Heydarifard, M.M. Nazhad, N. Dilbaghi, Nanotechnology-based water treatment strategies, J. Nanosci. Nanotechnol. 14 (2014) 1838–1858.
[24] Y. Boyjoo, H. Sun, J. Liu, V.K. Pareek, S. Wang, A review on photocatalysis for air treatment: from catalyst development to reactor design, Chem. Eng. J. 310 (2017) 537–559.
[25] A. Gnanaprakasam, V.M. Sivakumar, M. Thirumarimurugan, Influencing parameters in the photocatalytic degradation of organic effluent via nanometal oxide catalyst: a review, Indian J. Mater. Sci. 2015 (2015) 1–16.
[26] E. Pelizzetti, C. Minero, Metal oxides as photocatalysts for environmental detoxification, Comments Inorg. Chem. 15 (1994) 297–337.
[27] S. Nahar, M.F.M. Zain, A.A.H. Kadhum, H.A. Hasan, M.R. Hasan, Advances in

photocatalytic CO_2 reduction with water: a review, Materials 10 (2017).
[28] J. Singh, S. Uma, Efficient photocatalytic degradation of organic compounds by ilmenite $AgSbO_3$ under visible and UV light irradiation, J. Phys. Chem. C 113 (2009) 12483–12488.
[29] M.M. Khan, S.F. Adil, A. Al-Mayouf, Metal oxides as photocatalysts, J. Saudi Chem. Soc. 19 (2015) 462–464.
[30] R.A. Roca, J.C. Sczancoski, I.C. Nogueira, M.T. Fabbro, H.C. Alves, L. Gracia, L.P.S. Santos, C.P. de Sousa, J. Andres, G.E. Luz, E. Longo, L.S. Cavalcante, Facet-dependent photocatalytic and antibacterial properties of α-Ag_2WO_4 crystals: combining experimental data and theoretical insights, Cat. Sci. Technol. 5 (2015) 4091–4107.
[31] F. Chen, S. Li, Q. Chen, X. Zheng, P. Liu, S. Fang, 3D graphene aerogels-supported Ag and Ag@Ag_3PO_4 heterostructure for the efficient adsorption-photocatalysis capture of different dye pollutants in water, Mater. Res. Bull. 105 (2018) 334–341.
[32] J. Lv, K. Dai, J. Zhang, L. Lu, C. Liang, L. Geng, Z. Wang, G. Yuan, G. Zhu, In situ controllable synthesis of novel surface plasmon resonance-enhanced Ag_2WO_4/Ag/Bi_2MoO_6 composite for enhanced and stable visible light photocatalyst, Appl. Surf. Sci. 391 (2017) 507–515.
[33] Y. Huo, Z. Wang, J. Zhang, C. Liang, K. Dai, Ag SPR-promoted 2D porous g-C_3N_4/Ag_2MoO_4 composites for enhanced photocatalytic performance towards methylene blue degradation, Appl. Surf. Sci. 459 (2018) 271–280.
[34] T. Takahashi, S. Ikeda, O. Yamamoto, Solid-state ionics-solids with high ionic conductivity in the systems silver iodide-silver oxyacid salts, J. Electrochem. Soc. 119 (1972) 477–482.
[35] T. Takahashi, E. Nomura, O. Yamamoto, Solid state ionics-the ionic conductivity of the Ag_2S-$Ag_{1.70}Te$-Ag_X system (Ag_X; $Ag_4P_2O_7$, Ag_3PO_4 and $AgPO_3$), J. Appl. Electrochem. 3 (1973) 23–29.
[36] T. Yamada, H. Koizumi, Czochralski growth of $Ag_4P_2O_7$ crystals, J. Cryst. Growth 64 (1983) 558–562.
[37] T. Hirono, M. Fukuma, T. Yamada, Photoinduced effects in $Ag_4P_2O_7$ single crystals, J. Appl. Phys. 57 (1985) 2267–2270.
[38] H. Koizumi, T. Hirono, T. Yamada, Y. Miyamoto, N. Ogawa, M. Koizumi, M. Shimada, High-pressure polymorph of silver pyrophosphate $Ag_4P_2O_7$, Mater. Res. Bull. 21 (1986) 817–821.
[39] S. Ananthraj, K. Varma, K. Rao, Electrical properties of silver pyrophosphate glass, Solid State Ionics 27 (1988) 5–9.
[40] J. Zhao, Z. Ji, C. Xu, X. Shen, L. Ma, X. Liu, Hydrothermal syntheses of silver phosphate nanostructures and their photocatalytic performance for organic pollutant degradation, Cryst. Res. Technol. 49 (2014) 975–981.
[41] L. Song, Y. Li, H. Tian, X. Wu, S. Fang, S. Zhang, Synthesis of AgBr/$Ag_4P_2O_7$ composite photocatalyst and enhanced photocatalytic performance, Mater. Sci. Eng. B 189 (2014) 70–75.
[42] N. Fairley, CasaXPS: Spectrum Processing Software for XPS, AES and SIMS, Version 2.3.15, Casa Software Ltd., Cheshire, UK, 2009http://www.casaxps.com/.
[43] C.A. Schneider, W.S. Rasband, K.W. Eliceiri, NIH image to ImageJ: 25 years of image analysis, Nat. Methods 9 (2012) 671.
[44] F.S. Cunha, J.C. Sczancoski, I.C. Nogueira, V.G. de Oliveira, S.M.C. Lustosa, E. Longo, L.S. Cavalcante, Structural, morphological and optical investigation of β-Ag_2MoO_4 microcrystals obtained with different polar solvents, CrystEngComm 17 (2015) 8207–8211.
[45] S.A. Suthanthiraraj, R. Sarumathi, A new silver ion conducting SbI_3–$Ag_4P_2O_7$ nanocomposite solid electrolyte, Appl. Nanosci. 3 (2012) 501–508.
[46] D. Philip, B.L. George, G. Aruldhas, IR and polarized Raman spectra of $Na_4P_2O_7{\cdot}10H_2O$, J. Raman Spectrosc. 21 (1990) 523–524.
[47] N. Khay, A. Ennaciri, A. Rulmont, Structure and vibrational spectra of double diphosphates $TlLnP_2O_7$ (Ln = Dy, Ho, Y, Er, Yb), J. Raman Spectrosc. 32 (2001) 1052–1058.
[48] H. Brintzinger, R.A. Plane, Raman spectra of bis-diphosphate metal complexes in aqueous solution, Inorg. Chem. 6 (1967) 623–625.
[49] L. Guerbous, L. Gacem, Synthesis and luminescent properties of Eu^{3+} doped crystalline diphosphate $Na_2ZnP_2O_7$, Acta Phys. Pol. A 122 (2012) 535.
[50] J. Belkouch, L. Monceaux, F. Oudet, E. Bordes, P. Courtine, Synthesis and characterization of a new silver iron diphosphate, Mater. Res. Bull. 25 (1990) 1099–1107.
[51] B. Boonchom, N. Vittayakorn, Simple fabrication of polyhedral grain-like microparticle $Cu_{0.5}Zn_{0.5}HPO_4{\cdot}H_2O$ and porous structure $CuZnP_2O_7$, Ceram. Int. 38 (2012) 411–415.
[52] Y. Maréchal, The molecular structure of liquid water delivered by absorption spectroscopy in the whole IR region completed with thermodynamics data, J. Mol. Struct. 1004 (2011) 146–155.
[53] Z. Lou, B. Huang, Z. Wang, R. Zhang, Y. Yang, X. Qin, X. Zhang, Y. Dai, Fast-generation of Ag_3PO_4 concave microcrystals from electrochemical oxidation of bulk silver sheet, CrystEngComm 15 (2013) 5070.
[54] D. Fa, B. Yu, Y. Miao, Synthesis of ultra-long nanowires of nickel phosphate by a template-free hydrothermal method for electrocatalytic oxidation of glucose, Colloids Surf. A Physicochem. Eng. Asp. 564 (2019) 31–38.
[55] M. Hosseini-Sarvari, T. Ataee-Kachouei, F. Moeini, Preparation, characterization, and catalytic application of nano Ag/ZnO in the oxidation of benzylic C–H bonds in sustainable media, RSC Adv. 5 (2015) 9050–9056.
[56] L. Di, H. Yang, T. Xian, X. Chen, Facile synthesis and enhanced visible-light photocatalytic activity of novel p-Ag_3PO_4/n-$BiFeO_3$ heterojunction composites for dye degradation, Nanoscale Res. Lett. 13 (2018) 257.
[57] J.F. Moulder, J. Chastain, Handbook of X-ray Photoelectron Spectroscopy: A Reference Book of Standard Spectra for Identification and Interpretation of XPS Data, Physical Electronics Division, Perkin-Elmer Corporation, 1992.
[58] G. Balducci, L. Bravo Diaz, D.H. Gregory, Recent progress in the synthesis of nanostructured magnesium hydroxide, CrystEngComm 19 (2017) 6067–6084.
[59] L. Hu, L. Wu, M. Liao, X. Hu, X. Fang, Electrical transport properties of large, individual $NiCo_2O_4$ nanoplates, Adv. Funct. Mater. 22 (2012) 998–1004.
[60] F. Wu, C. Yu, W. Liu, T. Wang, J. Feng, S. Xiong, Large-scale synthesis of $Co_2V_2O_7$ hexagonal microplatelets under ambient conditions for highly reversible lithium storage, J. Mater. Chem. A 3 (2015) 16728–16736.
[61] F.C. Meldrum, H. Cölfen, Controlling mineral morphologies and structures in biological and synthetic systems, Chem. Rev. 108 (2008) 4332–4432.
[62] G.V. Franks, C. Tallon, A.R. Studart, M.L. Sesso, S. Leo, Colloidal processing: enabling complex shaped ceramics with unique multiscale structures, J. Am. Ceram. Soc. 100 (2017) 458–490.
[63] W. Ostwald, Lehrbuch der Allgemeinen Chemie, vol. 2, Engelmann, Leipzig, Germany, 1896 part 1. in, German.
[64] J.-L. Bredas, Mind the gap!, Mater. Horiz. 1 (2014) 17–19.
[65] S. Lee, G. Kim, H. Kim, B.Y. Choi, J. Lee, B.W. Jeong, J. Ihm, Y. Kuk, S.J. Kahng, Paired gap states in a semiconducting carbon nanotube: deep and shallow levels, Phys. Rev. Lett. 95 (2005) 166402.
[66] M.D. McCluskey, E.E. Haller, Dopants and Defects in Semiconductors, CRC Press, 2012.
[67] L. Tolvaj, K. Mitsui, D. Varga, Validity limits of Kubelka–Munk theory for DRIFT spectra of photodegraded solid wood, Wood Sci. Technol. 45 (2010) 135–146.
[68] Y. Xu, M.A. Schoonen, The absolute energy positions of conduction and valence bands of selected semiconducting minerals, Am. Mineral. 85 (2000) 543–556.
[69] S.R. Morrison, Electrochemistry at Semiconductor and Oxidized Metal Electrodes, (1980).
[70] D. Yu, Z.-D. Chen, F. Wang, S.-Z. Li, Study on electronegativity and hardness of the elements by density functional theory, Acta Phys. -Chim. Sin. 17 (2001) 15–22.
[71] S.K. Rout, L.S. Cavalcante, J.C. Sczancoski, T. Badapanda, S. Panigrahi, M. Siu Li, E. Longo, Photoluminescence property of powders prepared by solid state reaction and polymeric precursor method, Phys. B Condens. Matter 404 (2009) 3341–3347.
[72] R. Ahmed, M. Saif, Optical properties of Rhodamine B dye doped in transparent polymers for sensor application, Chin. J. Phys. 51 (2013) 511–521.
[73] G.S. Saini, S. Kaur, S.K. Tripathi, C.G. Mahajan, H.H. Thanga, A.L. Verma, Spectroscopic studies of rhodamine 6G dispersed in polymethylcyanoacrylate, Spectrochim. Acta A 61 (2005) 653–658.
[74] N. Narband, M. Uppal, C.W. Dunnill, G. Hyett, M. Wilson, I.P. Parkin, The interaction between gold nanoparticles and cationic and anionic dyes: enhanced UV-visible absorption, Phys. Chem. Chem. Phys. 11 (2009) 10513–10518.
[75] L. D'Ilario, A. Martinelli, Toluidine blue: aggregation properties and structural aspects, Model. Simul. Mater. Sci. Eng. 14 (2006) 581–595.
[76] T. Wu, G. Liu, J. Zhao, H. Hidaka, N. Serpone, Photoassisted degradation of dye pollutants. V. Self-photosensitized oxidative transformation of rhodamine B under visible light irradiation in aqueous TiO_2 dispersions, J. Phys. Chem. B 102 (1998) 5845–5851.
[77] Y. Zhao, C. Li, X. Liu, F. Gu, Highly enhanced degradation of dye with well-dispersed TiO_2 nanoparticles under visible irradiation, J. Alloys Compd. 440 (2007) 281–286.
[78] L. Bao, M. Meng, K. Sun, W. Li, D. Zhao, H. Li, M. He, Selective adsorption and degradation of rhodamine B with modified titanium dioxide photocatalyst, J. Appl. Polym. Sci. 131 (2014).
[79] L. Zou, X. Shen, Q. Wang, Z. Wang, X. Yang, M. Jing, Improvement of catalytic activity and mechanistic analysis of transition metal ion doped nanoCeO_2 by aqueous Rhodamine B degradation, J. Mater. Res. 30 (2015) 2763–2771.
[80] C. Chen, W. Zhao, J. Li, J. Zhao, H. Hidaka, N. Serpone, Formation and identification of intermediates in the visible-light-assisted photodegradation of sulforhodamine-B dye in aqueous TiO_2 dispersion, Environ. Sci. Technol. 36 (2002) 3604–3611.
[81] Y. Liu, J. Zhu, X. Liu, H. Li, A convenient approach of MIP/Co–TiO_2 nanocomposites with highly enhanced photocatalytic activity and selectivity under visible light irradiation, RSC Adv. 6 (2016) 69326–69333.
[82] L.S. Cavalcante, J.C. Sczancoski, N.C. Batista, E. Longo, J.A. Varela, M.O. Orlandi, Growth mechanism and photocatalytic properties of $SrWO_4$ microcrystals synthesized by injection of ions into a hot aqueous solution, Adv. Powder Technol. 24 (2013) 344–353.
[83] H. Al-Ekabi, N. Serpone, E. Pelizzetti, C. Minero, M.A. Fox, R.B. Draper, Kinetic studies in heterogeneous photocatalysis. 2. Titania-mediated degradation of 4-chlorophenol alone and in a three-component mixture of 4-chlorophenol, 2, 4-dichlorophenol, and 2, 4, 5-trichlorophenol in air-equilibrated aqueous media, Langmuir 5 (1989) 250–255.
[84] M. Mousavi, A. Habibi-Yangjeh, M. Abitorabi, Fabrication of novel magnetically separable nanocomposites using graphitic carbon nitride, silver phosphate and silver chloride and their applications in photocatalytic removal of different pollutants using visible-light irradiation, J. Colloid Interface Sci. 480 (2016) 218–231.
[85] S. Zhang, J. Li, X. Wang, Y. Huang, M. Zeng, J. Xu, In situ ion exchange synthesis of strongly coupled Ag@AgCl/g-C_3N_4 porous nanosheets as plasmonic photocatalyst for highly efficient visible-light photocatalysis, ACS Appl. Mater. Interfaces 6 (2014) 22116–22125.